



Bread-making synthesis of hierarchically Co@C nanoarchitecture in heteroatom doped porous carbons for oxidative degradation of emerging contaminants

Wenjie Tian^{a,1}, Huayang Zhang^{a,1}, Zhao Qian^{c,1}, Tianhong Ouyang^c, Hongqi Sun^{b,*}, Jingyu Qin^c, Moses O. Tadé^a, Shaobin Wang^{a,*}

^a Department of Chemical Engineering and CRC for Contamination Assessment and Remediation of the Environment (CRC CARE), Curtin University, GPO Box U1987, WA 6845, Australia

^b School of Engineering, Edith Cowan University, 270 Joondalup Drive, Joondalup, WA 6027, Australia

^c Key Laboratory for Liquid-Solid Structural Evolution & Processing of Materials (Ministry of Education), Shandong University, China

ARTICLE INFO

Keywords:

Porous carbon
Core/shell
Radicals
Doping
Advanced oxidation processes

ABSTRACT

Employing low-cost and abundant wheat flour, sodium bicarbonate, cysteine and cobalt nitrate as precursors, we for the first time present a facile one-pot pyrolysis strategy for homogeneous assembly of core-shell Co@C nanoparticles with nitrogen and sulfur into hierarchically porous carbons (Co-N-S-PCs). The samples are highly efficient for oxidative decomposition of *p*-hydroxybenzoic acid (HBA) and phenol. It was found that Co@C nanoparticles are crucial for the generation of singlet oxygen in advanced oxidation processes (AOPs), which works together with hydroxyl and sulfate radicals in efficient decomposition of HBA. Density functional theory (DFT) calculations disclose that electron transfer from metal Co to C shells greatly improves the Fermi level and chemical activity of the C atoms. The combination of Co-C interaction with N, S codoping further bring in catalytic active sites in the graphitic shells where the charge states of C atoms are increased. This template-free strategy is scalable to prepare highly efficient catalysts, including functional carbon materials modified with non-precious metal species or pure and well-dispersed porous core-shell nanoparticles for environmental or energy applications.

1. Introduction

The increasing demands for fresh drinking water supply have heightened a worldwide concern for growing water contamination by persistent organic pollutants (POPs) from agricultural, industrial and urban human activities [1]. For instance, non-biodegradable 4-hydroxybenzoic acid (HBA) and phenol have been widely detected in the wastewater [2,3], which can hardly decompose using conventional methods. Given that water quality is closely tied to the health of humankind and well-being of the planet Earth, sustainable treatment techniques are urgently required [1]. Among several available technologies, advanced oxidation processes (AOPs) are especially suitable for complete removal of organics and have attracted growing attention [4,5]. In essence, AOPs are based on generation of strong oxidizing radicals such as hydroxyl ($\cdot\text{OH}$), sulfate ($\text{SO}_4\cdot^-$), and singlet oxygen ($^1\text{O}_2$) [4], which are able to oxidize or react with most organic pollutants into low toxic compounds or final products of water and carbon

dioxide [6]. Compared with single $\cdot\text{OH}$ -based AOPs by traditional Fenton reaction, $\cdot\text{OH}$, $\text{SO}_4\cdot^-$, and $^1\text{O}_2$ can be simultaneously produced by the chemical activation of peroxydisulfate (HSO_5^- , PMS), making the process more efficient, non-selective and stable [7–9].

PMS can be activated via multifarious metal ions like Fe^{2+} , Co^{2+} , Ni^{2+} , Mn^{2+} , Ce^{3+} , and Ru^{3+} , among which Co^{2+} /PMS homogeneous system proves the best performance [10]. However, the excessive metal ions in solution are toxic and may have hazardous impacts on both the environment and public health [11]. Therefore, numerous approaches have been explored in the development of heterogeneous catalysts such as metal oxides and particularly carbon-based materials as green alternatives for PMS activation [12–19]. Recently, three-dimensional (3D) porous carbons have brought out new possibilities for efficient removal of organic pollutants in effluents, because of their fascinating advantages such as a large specific surface area (SSA), acceptable cost and desirable environmental benignity [20,21]. However, pristine carbons show limited catalytic efficiencies. In the last decades, various

* Corresponding authors.

E-mail addresses: h.sun@ecu.edu.au (H. Sun), shaobin.wang@curtin.edu.au (S. Wang).

¹ Authors contributed equally.

routes by introducing heteroatoms or metal species to the carbon system have been attempted for synthesizing functional catalysts with tailored features and enhanced properties [22,23]. N, B, S, and P are the commonly used heteroatoms [24]. It has been pointed out that, compared with single N or S doping, dual N, S doping into plain carbons can induce a synergistic effect for more efficient catalysis [24,25]. Besides, the earth-abundant element of cobalt can catalyze the formation of more ordered sp^2 -hybridized carbon, which works more effectively for PMS activation compared with the inactive sp^3 -C [9,26].

Herein we first demonstrate one-pot pyrolysis of wheat flour, sodium bicarbonate, and cysteine into nitrogen and sulfur co-doped three-dimensional (3D) porous carbons. With a cobalt precursor, Co core@N-S codoped C-shell nanoparticles embedded uniformly in hierarchically porous structures (Co-N-S-PCs) can be fabricated. Wheat flour is chosen as the carbon source because it is cheap, abundant and reproducible. Using sodium bicarbonate as a porogen is originally inspired by the fact that it can act as a swelling agent in bread-making processes. Cysteine, a flour dough improver, can supply N, S atoms and there is a complexation between cobalt (II) and cysteine [27,28], which is beneficial for self-assembly and homogenous distribution of cobalt (II) in a molecular dimension. The resulting Co-N-S-PCs are proven to be excellent catalysts in PMS activation for complete and efficient HBA and phenol decomposition. More importantly, density functional theory (DFT) calculations were carried out to gain an insight into the active sites introduced by Co@C structure and N, S dual doping in the graphitic shells. The scalable and economic synthesis route endows these materials with numerous opportunities for large-scale production and promising application in environmental and energy catalysis.

2. Experimental section

2.1. Chemical reagents

Wheat flour was provided by a local supermarket, Coles in Australia, containing starch, protein (11 wt.%) and trace sodium. Sodium bicarbonate ($\geq 99.7\%$), L-cysteine ($\geq 98.0\%$), cobalt nitrate hexahydrate (99.9%), peroxymonosulfate ($\geq 99.0\%$), hydrochloric acid (36.5%), methanol ($\geq 99.9\%$), p-hydroxybenzoic acid (HBA, $\geq 97.0\%$), phenol (99.9%), 2,2,6,6-tetramethyl-4-piperidinol (TMP, 98%) and 5,5-dimethyl-1-pyrroline N-oxide (DMPO, $\geq 97.0\%$) were received from Sigma-Aldrich. All the chemicals were used directly without further purification.

2.2. Sample synthesis

For a typical fabrication of Co-N-S-PCs, wheat flour (2 g) was first added in 50 mL deionized water by magnetic stirring at 25 °C. Then, 3 g sodium bicarbonate, and 0.3 g cysteine were fully dissolved in 80 mL deionized water, which was mixed with the flour solution. Subsequently, 0.15 g cobalt nitrate hexahydrate dissolved in 10 mL deionized water was added to the above solution dropwisely. After drying at 80 °C under constant stirring, the as-obtained homogeneous mixture was subjected to pyrolysis at 700, 800 and 850 °C for 2 h, respectively, with a ramp rate of 5 °C/min under a N_2 flow in a tube furnace. The carbonized materials were ground to powders, followed by washing with water and ethanol, and then dried in an oven. Accordingly, the samples obtained at different temperatures were denoted as Co-N-S-PC 700, Co-N-S-PC 800 and Co-N-S-PC 850, respectively. For comparison, blank carbon was prepared by carbonization of wheat flour at 700 °C, while N-S co-doped porous carbon was obtained by the pyrolysis of flour, sodium bicarbonate and L-cysteine at 700 °C without cobalt nitrate hexahydrate (N-S-PC 700). Co-N-S-PC 700 (Acid washing) was acquired by etching Co-N-S-PC 700 with 5 wt.% HCl solution for 10 h. After that, the sample was washed alternately with water and ethanol, and finally dried in an oven.

2.3. Characterizations

Thermogravimetric analysis (TGA) and differential thermogravimetry analysis (DTG) were conducted on a thermogravimetric analysis instrument (TGA/DSC1 STAR^e system, METTLER-TOLEDO). X-ray diffraction (XRD) patterns were acquired on a Bruker D8-Advanced X-ray instrument. Raman spectroscopy was performed on a WITec alpha 300RA+ system. Morphologies of the samples were revealed on a scanning electron microscope (FEI Verios XHR 460, SEM) with an energy dispersive spectrometer (EDS) and a transmission electron microscope (JEOL 2100, TEM). High angle annular dark field scanning TEM (HAADF-STEM) images and corresponding energy-dispersive X-ray spectroscopy (EDX) elemental mapping were achieved by FEI Titan G2 80-200 TEM/STEM. X-ray photoelectron spectroscopy (XPS) was obtained with a Kratos AXIS Ultra DLD system under ultra-high vacuum (UHV) condition by monochromated Al-K α X-rays. The specific surface area (SSA) and pore size distribution of the samples were determined by N_2 adsorption/desorption at -196 °C on a Micromeritics Tristar 3000. Electron paramagnetic resonance (EPR) was performed during HBA oxidation on a Bruker EMS-plus instrument to detect free radicals, with DMPO or TMP as a spin-trapping agent and the results were analyzed by Xeon software (Bruker).

2.4. Adsorption and AOP procedures

Adsorption tests were conducted at 25 °C by dispersing 10 mg of the resulting samples in 150 mL HBA or phenol solutions (20 mg L^{-1}), which means the loading amount of the adsorbent is 0.066 g/L. At certain time intervals, 1 mL of the solution was withdrawn and filtered. The concentrations of HBA or phenol were determined by an ultra-high performance liquid chromatography (UHPLC).

Typical HBA or phenol oxidation tests were also carried out at 25 °C unless otherwise mentioned. The catalyst samples (0.066 g/L) and peroxymonosulfate (HSO_5^- , PMS, 6.5 mM) were added together in HBA or phenol (20 mg L^{-1}) solution to initiate the reaction. After certain reaction time, 1.0 mL filtered solution was mixed instantly with 0.5 mL methanol to stop the reaction. All the experiments were repeated with reproducible results.

3. Results and discussion

3.1. Material characterizations

TGA and DTG curves provided in Fig. 1a reveal the thermal decomposition of the precursor mixture to the synthesis of Co-N-S-PCs in Ar environment. The initial weight loss below 110 °C is due to water evaporation [29]. The carbonization and decomposition of the precursors proceed in a temperature range between 190 and 300 °C as reflected by a sharp weight loss in the curves. The thermal degradation is mild between 300–750 °C. Notably, there is a dramatic weight loss over 800 °C, which also means the sharp reduction of sample yield.

Based on the TGA results, typical pyrolysis temperatures of 700, 800 and 850 °C were selected to prepare Co-N-S-PC 700, Co-N-S-PC 800 and Co-N-S-PC 850, accordingly. For comparison, N-S-PC 700 was fabricated without a cobalt precursor. XRD pattern of N-S-PC 700 shows two broad peaks at 23° and 43°, respectively, which imply the formation of nanoscale graphitic units assembled in topological disorder (Fig. 1b) [30,31]. Superimposed upon the two broad peaks, sharp narrow peaks located at 26.2° and 44.3° start to appear in Co-N-S-PC 700, and their intensities increase in Co-N-S-PC 800. The two sharp peaks are assigned to the (002) and (101) planes of graphite (PDF#41-1487), respectively, indicating the development of graphitic domains on an amorphous C matrix. The broad peaks nearly disappear in Co-N-S-PC 850, which suggests the removal of amorphous carbon over 850 °C. The cobalt species in Co-N-S-PCs accord well with the (111), (101), (200) and (220) planes of cubic cobalt (PDF#15-0806). D/G intensity ratio (I_D/I_G

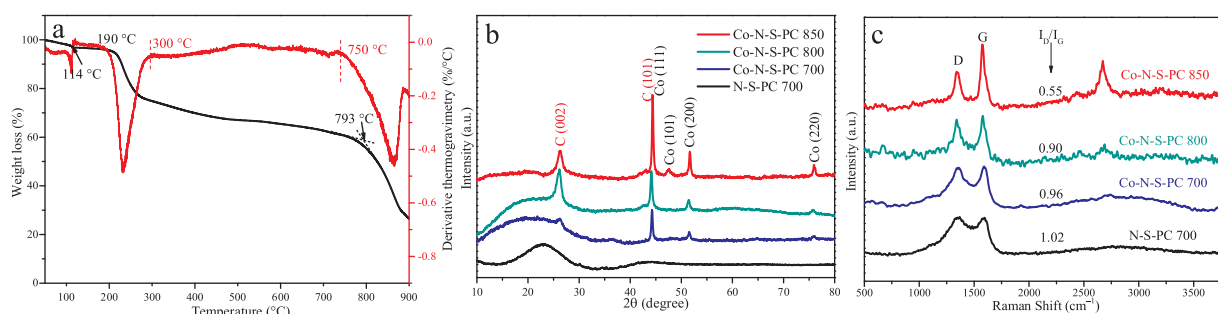


Fig. 1. a) TGA and DTG curves of the precursor mixture conducted in argon atmosphere, b) XRD patterns and c) Raman spectra of the synthesized materials.

in the Raman spectra in Fig. 1c) of the samples decreases continuously from N-S-PC 700, Co-N-S-PC 700 to Co-N-S-PC 800, declaring an increasing graphitized carbon ratio induced by cobalt catalysis at rising synthesis temperatures. Consistent with XRD results, Co-N-S-PC 850 demonstrates a significantly enhanced graphitic degree with a much lower I_D/I_G ratio compared to the other samples.

Fig. S1a shows a representative scanning electron microscopy (SEM) image of blank carbon with nonporous morphology. In contrast, a hierarchically porous structure is developed on N-S-PC 700 (Fig. S1b), which can be primarily attributed to the gas and water vapor release from the decomposition of cysteine and sodium bicarbonate during the pyrolysis process. SEM and transmission electron microscopy (TEM) images of Co-N-S-PC 700 and 800 in Figs. 2 and S1 reveal 3D porous networks in which granular nanoparticles are homogeneously embedded in the pores. The elemental mapping analysis in SEM indicates that the granular particles are cobalt nanoparticles (Fig. S2). High-resolution transmission electron microscopy (HRTEM) images of the porous

carbons, N-S-PC 700, Co-N-S-PC 700 and Co-N-S-PC 800, disclose the nature of amorphous carbon constructed of scrambled graphitic layers (Figs. 2d and S3a, b). HRTEM analysis indicates that the granular cobalt nanoparticles are composed of outer continuous graphitic layers with interspacing of 0.34 nm ((002) plane) and cubic Co core ((111) plane), generating a Co@C core-shell structure (Figs. 2e, f and S3c). It is noticed in Figs. 2a and b that the 3D porous carbon matrix of Co-N-S-PC 800 is thinner than that of Co-N-S-PC 700. Figs. 2c, S1e, and S3d further display that Co-N-S-PC 850 mainly consists of Co@C nanoparticles. This means that the porous carbon skeletons can be gradually decomposed until completely removed at high temperatures, and thus this facile approach can be used to obtain well-dispersed Co@C nanoarchitecture. This helps explain the highest graphitization degree in Co-N-S-PC 850 as suggested by XRD and Raman data. HAADF-STEM images display that C, N, O, S distribute uniformly in N-S-PC 700 (Fig. S3e). For other carbons, Co-N-S-PC 700, 800 and 850, HAADF-STEM analysis (Figs. 2g, h and S3f) shows the presence of C, N, O, S in the porous structure and

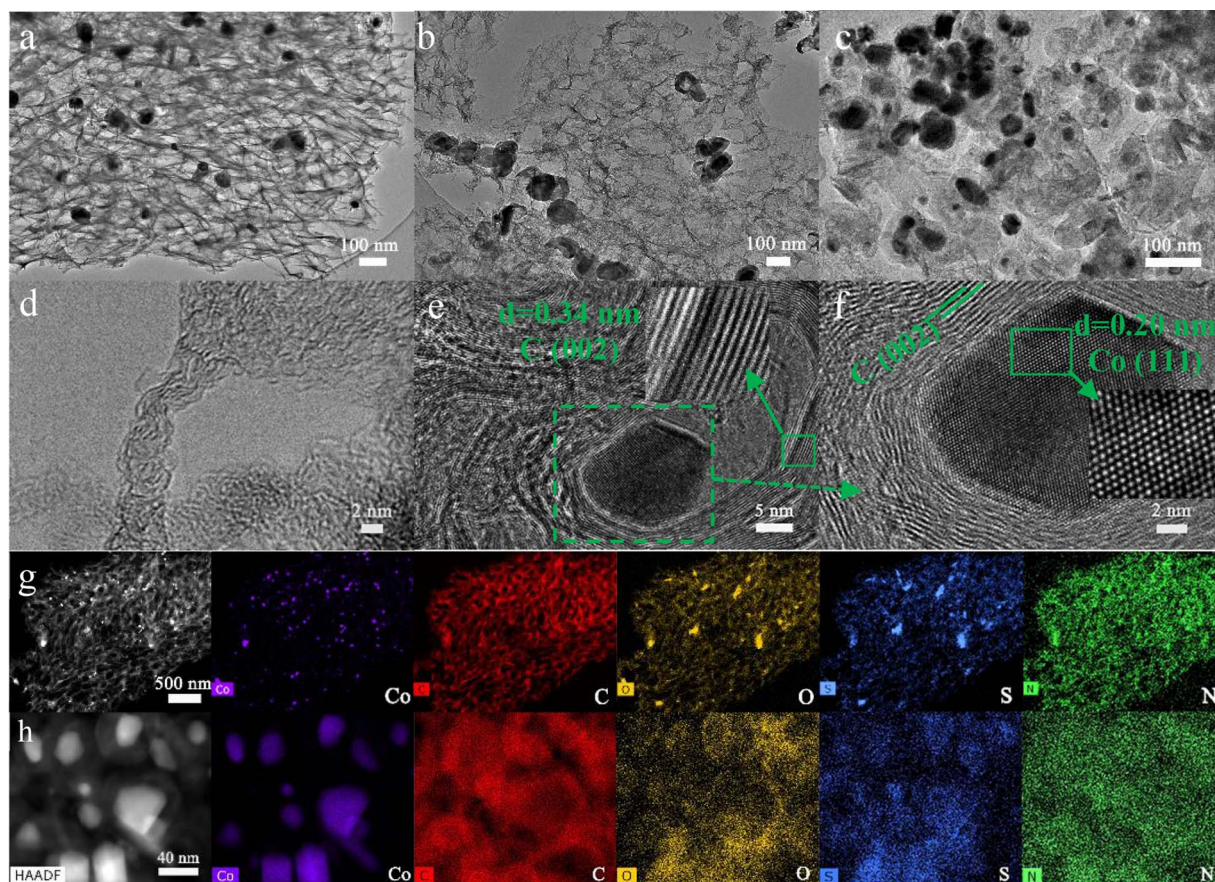
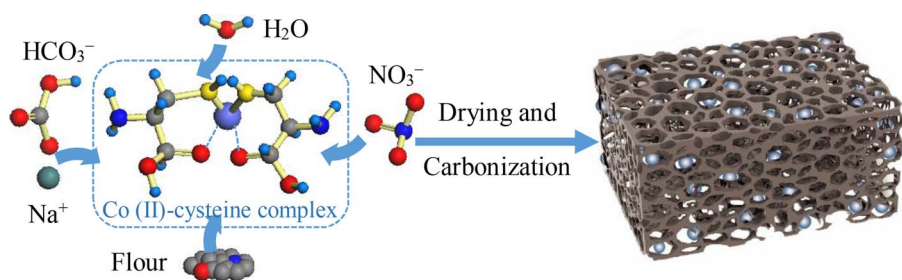


Fig. 2. TEM images of a) Co-N-S-PC 700, b) Co-N-S-PC 800 and c) Co-N-S-PC 850. d–f) HRTEM images of Co-N-S-PC 800. High angle annular dark field scanning TEM images (HAADF-STEM) of g) Co-N-S-PC 700 and h) Co-N-S-PC 850 with energy-dispersive X-ray spectroscopy (EDX) elemental mapping images.



Scheme 1. Formation process of Co-N-S-PCs.

the carbon shells in Co@C nanoparticles.

The formation mechanism of the unique structure of Co-N-S-PCs is proposed in Scheme 1. After all the precursors are dissolved in water, the interactions of cobalt cations (II) with sulfur and carboxylate groups in cysteine will first lead to Co(II)-cysteine complexes, as evidenced by numerous studies [27,28]. The strong hydrogen-bond or electrostatic interactions among the precursors (Na^+ , HCO_3^- , flour, NO_3^- and Co (II)-cysteine complexes) then facilitate an uniform self-assembly during the water evaporation process. After drying and carbonization of the mixture, Co@C nanoparticles are in-situ generated in the pores of 3D porous carbon. With higher synthesis temperatures over 850 °C, the amorphous porous carbon matrix can be removed, resulting in dispersive Co@C nanoparticles.

X-ray photoelectron spectroscopy (XPS) results are summarized in Figs. 3, S4 and Table 1. The nitrogen in blank carbon originates from carbonization of proteins in wheat flour. N-S-PC 700 and Co-N-S-PC 700 possess similar N and S doping levels. There are slight decreases of N, O and S contents from Co-N-S-PC 700 to Co-N-S-PC 850 with elevating pyrolysis temperatures. Since wheat flour contains trace amount of sodium compounds and sodium bicarbonate was used as the

porogen, all the samples have sodium residuals. Surface cobalt contents were measured to be 0.55–1.5 at.% in Co-N-S-PCs. To evaluate the weight ratio of cobalt, TGA tests of the samples were performed under air (Fig. 3a). The thermal decomposition completed at above 650 °C. The residual weight in N-S-PC 700 (15 wt.%) originates from sodium residuals, which was utilized to estimate cobalt content in Co-N-S-PCs. After compensating sodium compound weight percentage, Co-N-S-PC 700, Co-N-S-PC 800 and Co-N-S-PC 850 present about 7, 11 and 33 wt. % cobalt compound contents, respectively. The residual cobalt form should be Co_3O_4 oxidized from Co calcination under air. Therefore, the weight ratios of Co were further calculated to be 1.72, 2.70 and 8.09 wt. % in Co-N-S-PC 700, Co-N-S-PC 800 and Co-N-S-PC 850, respectively. From XPS, the Co contents in weight were also obtained as 3.38, 2.57 and 6.78 wt.% for Co-N-S-PC 700, Co-N-S-PC 800 and Co-N-S-PC 850, respectively. As shown, the values are similar to the data from TGA. High resolution Co 2p spectra in Co-N-S-PCs feature Co $2p_{3/2}$ at 778.1 eV and Co $2p_{1/2}$ at 793.1 eV with an energy separation of 15.0 eV, typical as metallic Co (Fig. 3b) [32,33]. Fig. 3c confirms that doping N atoms exist in the form of pyridinic (398 eV), pyrrolic (400 eV), quaternary (401 eV) and oxidized nitrogen (405 eV)

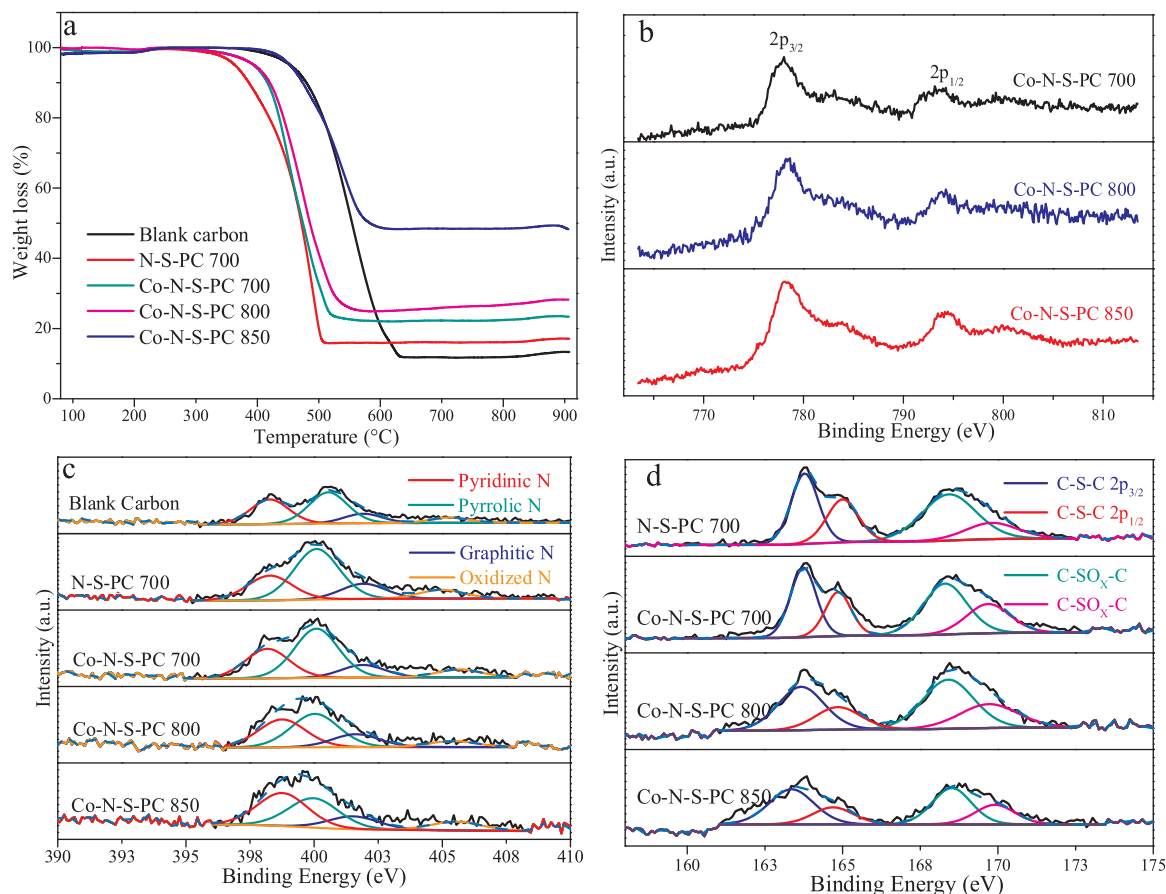


Fig. 3. a) TGA tests of the samples conducted in air. XPS core level spectra of b) Co 2p, c) N 1s and d) S 2p.

Table 1
Chemical compositions and textural properties of the samples.

	C/at. %	N/at. %	O/at. %	S/at. %	Na/at. %	Co/at. %	Co/wt. %	SSA ^a /m ² g ⁻¹	V _t ^b /cm ³ g ⁻¹	V _{mic} ^c /cm ³ g ⁻¹
Blank carbon	90.05	1.99	7.78	–	0.18	–	–	5	0.005	–
N-S-PC 700	88.80	1.60	8.46	0.42	0.72	–	–	332	0.25	0.12
Co-N-S-PC 700	87.39	1.89	9.03	0.52	0.43	0.74	1.72	505	0.42	0.20
Co-N-S-PC 800	92.29	1.17	5.51	0.34	0.14	0.55	2.70	734	0.58	0.21
Co-N-S-PC 850	91.64	0.91	5.39	0.29	0.27	1.50	8.09	379	0.50	0.049

^a Specific surface area calculated by the BET method.

^b Total pore volume at P/P₀ = 0.99.

^c Micropore volume calculated using the t-plot method.

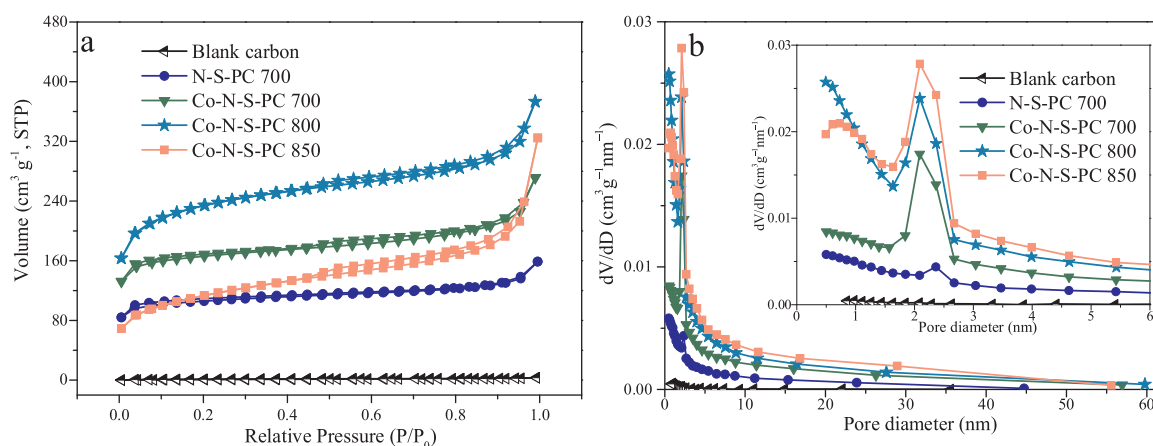


Fig. 4. a) N₂ sorption isotherms and b) BJH pore size distributions of the as-synthesized catalysts.

[20,34,35]. For S atoms (Fig. 3d), typical thiophene-S peaks arising from the S 2p_{3/2} (164 eV) and S 2p_{1/2} (165 eV) multiplets are observed, in together with oxidizing SO_x centered at around 168 and 170 eV [20,33].

It is noticeable that N₂ sorption behaviors on samples vary due to different precursors and synthesis temperatures (See Table 1 and Fig. 4). The type I isotherm of N-S-PC 700 with saturation at high-pressure reveals that the material contains a large fraction of micropores [31]. Co-N-S-PCs display type IV isotherms with the capillary condensation steps, suggesting the well-developed mesoporosity after cobalt introduction. The pore size distribution curve indicates that N-S-PC 700 has a hierarchically porous structure with micropores and mesopores. Apart from the micropores and mesopores, a small amount of macropores were also developed in Co-N-S-PCs.

N-S-PC has a SSA of 332 m² g⁻¹, in contrast to blank carbon (5 m² g⁻¹). This result proves that sodium bicarbonate and cysteine are crucial in forming the large porosity in these systems. Co-N-S-PC 700 has a 1.5-time-larger SSA than N-S-PC 700, which seems to be originated from a better cooperative interaction among all the precursors promoted by cobalt ions in the self-assembly process, as described in Scheme 1. The maximal SSA and pore volume are recorded on Co-N-S-PC 800, while there is a drastic decline in micropore volume and SSA in Co-N-S-PC 850.

3.2. Environmental application of the as-synthesized materials for HBA and phenol removal

With N, S co-doping and Co@C nanoparticles in hierarchical porous structure, the developed Co-N-S-PCs are very appealing for adsorption and catalysis. As an example, we used them as catalysts for PMS activation in AOPs at a low catalyst loading of 0.066 g/L. Since adsorption is usually occurring along with AOPs, the adsorptive ability was also evaluated (Fig. 5a). Co-N-S-PC 800 showed the highest HBA adsorption (17%) due to the highest SSA, whereas the adsorption on other

materials was less than 10%. For AOPs, PMS alone generated trace degradation of HBA. With N-S-PC 700/PMS in the solution, HBA removal reached 60% degradation in 150 min. In contrast, complete HBA removal was achieved in 60 min for Co-N-S-PC 700/PMS, while 45 min for both Co-N-S-PC 800/PMS and Co-N-S-PC 850/PMS. It is therefore concluded that Co@C nanoparticles play a key role for efficient HBA removal. Ascribed to incremental proportion of Co@C structure in the samples, the reaction rate constants (k) of N-S-PC 700, Co-N-S-PC 700, Co-N-S-PC 800 and Co-N-S-PC 850 show an increasing trend, which were estimated to be 0.0047, 0.058, 0.068 and 0.11 min⁻¹, respectively, by the first-order kinetic model (Eq. (1)) [36]. The reaction efficiency in Co-N-S-PC 700/PMS system was elevated by about 12 times compared with N-S-PC 700/PMS in HBA oxidation.

$$\ln(C/C_0) = -kt \quad (1)$$

Where C₀ is the initial HBA concentration; C is the concentration of HBA at different time intervals (t); k is defined as the reaction rate constant.

Given that the production yield of Co-N-S-PCs decreases with rising temperatures especially at 850 °C as perceived from Fig. 1a, Co-N-S-PC 700 is more suitable for large-scale production with comparable catalytic performance to Co-N-S-PC 800 and Co-N-S-PC 850. Fig. 5b exhibits that a higher reaction solution temperature leads to a higher HBA oxidation efficiency. Compared to 60 min degradation time at 25 °C, HBA removal completed in 45 min at 35 °C while 30 min at 45 °C by Co-N-S-PC 700/PMS. With rising temperatures, the rate constants increase steadily from 0.058, 0.090 to 0.19 min⁻¹. Based on the Arrhenius correlation, the activation energy (E_a) of Co-N-S-PC 700 for the catalytic HBA degradation was calculated to be 44.5 kJ mol⁻¹. Fig. S5a shows the performance of recycled Co-N-S-PC 700 in HBA degradation. A deactivation occurred in the catalytic performance in the second run, yet 98% of HBA could still be removed in 120 min by the catalyst and about 76% of HBA was degraded in the third use. No obvious changes in the structure of Co-N-S-PC 700 were observed in SEM images before and after the third use (Fig. S6a, b). However, STEM analysis (Fig. S6c)

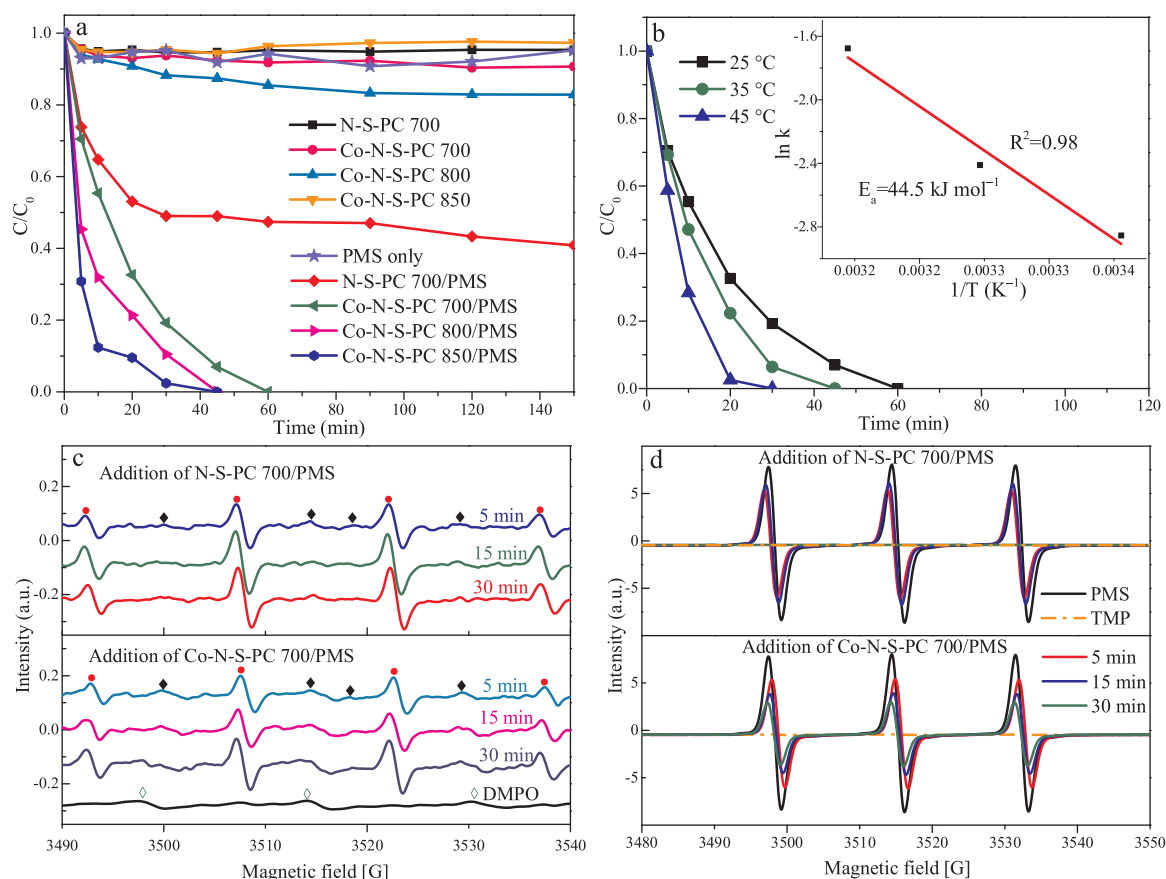


Fig. 5. a) HBA removal by adsorption and AOPs, b) influence of different reaction temperatures on HBA degradation for Co-N-S-PC 700/PMS, c) EPR tests on $\cdot\text{OH}$ and $\text{SO}_4\cdot^-$ during HBA degradation (DMPO- $\cdot\text{OH}$ —●; DMPO- $\text{SO}_4\cdot^-$ —◆; DMPOX—◇), and d) EPR measurements for $^1\text{O}_2$ during HBA degradation.

indicated that the contents of N and S elements decreased obviously in the sample after the third run. XPS was conducted on Co-N-S-PC 700 after the third-run test, which further proved an increased O content and decreased N and S contents. This is understandable by considering the strong oxidation environment in AOPs. Combined with our previous studies, it is deduced that the changes in surface chemistry and coverage of intermediates on the catalyst surface are mainly responsible for the deterioration of performance in recycling tests [26,37]. Stability tests were also carried out on Co-N-S-PC 800/PMS and Co-N-S-PC 850/PMS (Fig. S5b and c), which provided 100% degradation efficiency on HBA in the second run, while 58% and 52% HBA removal efficiencies in 120 min in the third run, respectively.

Not only effective for HBA removal, Co-N-S-PCs also displayed a highly efficient catalytic activity in degradation of other organic pollutants such as phenol solution. Fig. S8 shows that Co-N-S-PCs provided about 40% of phenol adsorption. Co-N-S-PC 700 and 800 achieved 100% phenol degradation in 1 h, compared to complete degradation in 10 min by Co-N-S-PC 850/PMS.

3.3. Mechanistic study in AOPs

As discussed before, AOPs are based on the generation of highly reactive radicals. As a strong oxidant, hydroxyl radical ($\cdot\text{OH}$) is able to react almost non-selectively with most organic pollutants [38]. Compared to $\cdot\text{OH}$, sulfate radical ($\text{SO}_4\cdot^-$) reacts more efficiently and selectively with organic compounds with a longer half-life period [5]. In addition, we recently proved that $^1\text{O}_2$ contributed significantly to the catalytic degradation of phenolic compounds [7,36]. To elucidate the various catalytic processes in N-S-PC 700/PMS and Co-N-S-PC 700/PMS, we adopted in-situ electron paramagnetic resonance (EPR) to inspect the radical generation and evolution during HBA degradation.

DMPO is effective to capture signals of $\cdot\text{OH}$ and $\text{SO}_4\cdot^-$ and the results are provided in Fig. 5c. Both N-S-PC 700/PMS and Co-N-S-PC 700/PMS produced a mass of $\cdot\text{OH}$ throughout 30 min reaction time. $\text{SO}_4\cdot^-$ signals were also detected in both systems and the intensities slightly dropped from 5 to 30 min reaction time due to the potential consumption by AOPs. Despite little difference in terms of $\cdot\text{OH}$ and $\text{SO}_4\cdot^-$, a clear distinction in singlet oxygen ($^1\text{O}_2$) activation was observed between the two systems (Fig. 5d). Utilizing TMP as the trapping agent, three typical lines with equal intensities can be detected for $^1\text{O}_2$. It was reported that $^1\text{O}_2$ can be produced by the self-decomposition of PMS at a low rate [39]. In N-S-PC 700/PMS system, the intensity of $^1\text{O}_2$ declined and went to zero in 30 min consumed by the reactive degradation of HBA, implying that N-S-PC 700 is inactive to activate PMS in continuous $^1\text{O}_2$ production. In contrast, there were strong $^1\text{O}_2$ signals after adding Co-N-S-PC 700/PMS into HBA solution even after 30 min reaction. Therefore, it is reasonable to assert that Co@C nanoparticles in Co-N-S-PCs promote PMS activation to produce $^1\text{O}_2$ radicals, which work together with $\cdot\text{OH}$ and $\text{SO}_4\cdot^-$ for the efficient decomposition of HBA.

To probe the roles of $\cdot\text{OH}$, $\text{SO}_4\cdot^-$ and $^1\text{O}_2$ in HBA degradation by Co-N-S-PC 700/PMS, quenching experiments were further carried out (Fig. S9a). Ethanol (Ethanol: PMS = 1000: 1) was chosen to quench $\cdot\text{OH}$ and $\text{SO}_4\cdot^-$ while NaN_3 (3 mM) was adopted as the scavengers for $^1\text{O}_2$. The concentration of quenching agents was determined according to our recent study [7]. Both ethanol and NaN_3 quenching affected the degradation efficiency obviously, proving that $\cdot\text{OH}$, $\text{SO}_4\cdot^-$ and $^1\text{O}_2$ work together for effective HBA decomposition.

The better catalytic activity of Co-N-S-PC 700 promoted by Co@C nanoparticles may originate from three characteristics: (i) the graphitic carbon shell contains a high ratio of $\text{sp}^2\text{-C}$, which is more active than $\text{sp}^3\text{-C}$ for PMS activation [9,26]; (ii) N and S co-doping can exert a

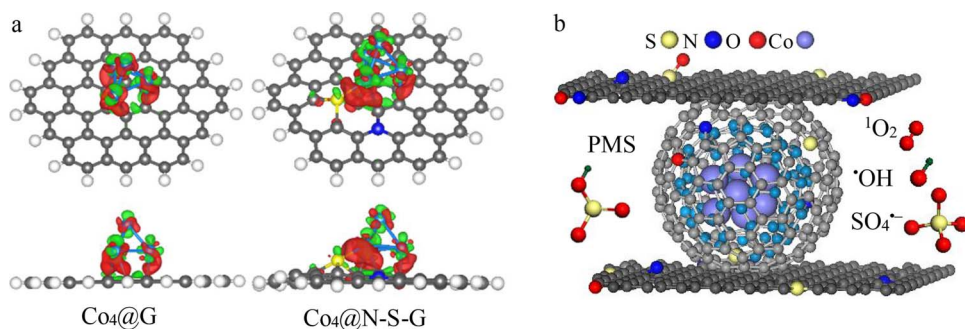


Fig. 6. a) The different charge densities in Co₄@G and Co₄@N-S-G. The green regions illustrate charge depletion while red regions indicate charge accumulation. The isovalue = 0.006 e/Å³. b) A schematic illustration for the AOPs in Co-N-S-PCs/PMS system. (For interpretation of the references to color in this figure legend, the reader is referred to the web version of this article.)

synergistic effect and make a further enhancement in the catalytic activity of the carbon shells. This is owing to the more active sites after N and S codoping and the redistribution of spin and charge densities of C [24,40]; (iii) encapsulated cobalt nanoparticles might facilitate the catalysis by altering the electron densities of C in the external carbon shells. To inspect the role of cobalt in catalysis, Co-N-S-PC 700 (Acid washing) was prepared and tested for HBA degradation (Fig. S9b). Although SEM characterization (Fig. S9c, d) indicates that Co was not fully removed by the acid washing due to the protection of the outer carbon shells, the catalytic performance in HBA removal was impaired obviously. It is noted that a better reaction occurred at the initial stage, which can be attributed to the improved porous structure and surface for the adsorption and carbon catalysis. Overall, only 80% of HBA was removed in 120 min. This result suggests that the Co cores in Co@C nanoparticles are essential for efficient AOPs.

3.4. DFT calculations

DFT calculations were adopted to better understand the nature of active sites induced by N, S codoped Co@C nanoparticles. Since the carbon layers covering cobalt cores have been proven to be graphitic layers, three models were constructed (Fig. S10) including graphene patch (designated as G), Co₄ cluster on graphene patch (Co₄@G) and Co₄ cluster on N, S codoped graphene patch (Co₄@N-S-G).

The total density of states (TDOS) of C atoms in three models are presented in Fig. S11. Co-C interaction and the dual doping of N and S introduce asymmetrical TDOS in the spin up and down modes. Apparently, the density of states increases significantly in the energy range of 4.3–2.0 eV, suggesting an elevated catalytic activity [24]. Promoted by electron transfer from Co₄ cluster to C as verified by C1-C6 atoms in Table S1, the Fermi level of the system advances by 1.39 eV towards the vacuum level in Co₄@G, while 1.36 eV in Co₄@N-S-G compared with G. This change decreases the local work function and increases chemical activity of the functionalized region in graphene [23]. After N, S doping, the spin down TDOS near the Fermi level in Co₄@N-S-G is higher than that in Co₄@G system, which is expected to further elevate the catalytic reactivity of carbon in the doped area. Fig. 6a illustrates the charge redistribution caused by Co-C interaction and N, S atom co-doping. The charge accumulates between the C and Co atoms in Co₄@G model, which means the strong interaction between them. After N, S doping, charge accumulation between S and Co atoms turns stronger. Table S1 provides the charge states of several typical atoms in the three systems. Single Co-C interaction leads to the decreased charge states in C1-C6 atoms while after N, S dual-doping, the charge states in the adjacent C2 and C6 atoms are positively increased, which can serve as catalytic active sites [24]. We believe that the positively charged C atoms and the modified chemical reactivity by introducing Co@N, S codoped C promote the adsorption and activation of PMS to generate effective radicals including ¹O₂, [•]OH, and SO₄^{•-}, leading to considerably enhanced HBA degradation, as depicted in Fig. 6b.

4. Conclusions

A template-free, bread-making inspired strategy was applied to assemble N, S co-doped core-shell Co@C nanoparticles into hierarchical porous carbons. The porous carbon matrix can be removed to obtain evenly-distributed porous Co@C nanostructure in Co-N-S-PC 850. The Co-N-S-PCs exhibit an excellent activity in PMS activation for HBA and phenol oxidation. Compared with N-S-PC 700/PMS, the reaction rate in HBA degradation by Co-N-S-PC 700/PMS is enhanced by about 12 times high. Co@C nanoparticles facilitate generation of ¹O₂ in AOPs, which works together with [•]OH and SO₄^{•-} in efficient decomposition of HBA by Co-N-S-PCs. DFT calculations prove that Co-C interaction improves the Fermi level and chemical activity of the functionalized C atoms. With the synergistic effect of Co-C interaction and N, S co-doping, the charge states of some C atoms are positively elevated to act as active sites for catalysis. Considering the diversity of carbon sources and non-precious metal species, the proposed method may offer a facile method to design hierarchical nanostructures with enhanced performance in environment and energy related catalysis.

Acknowledgements

This work is partially supported by the Australian Research Council (DP150103026). The authors thank the material characterization assistance from The University of Western Australia Centre for Microscopy, Characterisation and Analysis, and also help from the WA X-Ray Surface Analysis Facility of Curtin University for XPS tests.

Appendix A. Supplementary data

Supplementary data associated with this article can be found, in the online version, at <http://dx.doi.org/10.1016/j.apcatb.2017.11.056>.

References

- [1] M.A. Shannon, P.W. Bohn, M. Elimelech, J.G. Georgiadis, B.J. Marinas, A.M. Mayes, Science and technology for water purification in the coming decades, *Nature* 452 (2008) 301–310.
- [2] F.J. Rivas, F.J. Beltrán, J. Frades, P. Buxeda, Oxidation of p-hydroxybenzoic acid by Fenton's reagent, *Water Res.* 35 (2001) 387–396.
- [3] J. Beltrán-Heredia, J. Torregrosa, J.R. Domínguez, J.A. Peres, Comparison of the degradation of p-hydroxybenzoic acid in aqueous solution by several oxidation processes, *Chemosphere* 42 (2001) 351–359.
- [4] K.E. O'Shea, D.D. Dionysiou, Advanced oxidation processes for water treatment, *J. Phys. Chem. Lett.* 3 (2012) 2112–2113.
- [5] P.D. Hu, M.C. Long, Cobalt-catalyzed sulfate radical-based advanced oxidation: a review on heterogeneous catalysts and applications, *Appl. Catal. B: Environ.* 181 (2016) 103–117.
- [6] W.H. Glaze, J.-W. Kang, D.H. Chapin, The chemistry of water treatment processes involving ozone, hydrogen peroxide and ultraviolet radiation, *Ozone: Sci. Eng.* 9 (1987) 335–352.
- [7] P. Liang, C. Zhang, X. Duan, H. Sun, S. Liu, M.O. Tade, S. Wang, An insight into metal organic framework derived N-doped graphene for the oxidative degradation of persistent contaminants: formation mechanism and generation of singlet oxygen from peroxymonosulfate, *Environ. Sci. Nano* 4 (2017) 315–324.
- [8] E. Saputra, S. Muhammad, H. Sun, H.-M. Ang, M.O. Tade, S. Wang, Shape-controlled activation of peroxymonosulfate by single crystal α -Mn₂O₃ for catalytic

- phenol degradation in aqueous solution, *Appl. Catal. B: Environ.* 154–155 (2014) 246–251.
- [9] H.Q. Sun, S.Z. Liu, G.L. Zhou, H.M. Ang, M.O. Tade, S.B. Wang, Reduced graphene oxide for catalytic oxidation of aqueous organic pollutants, *ACS Appl. Mater. Interfaces* 4 (2012) 5466–5471.
 - [10] G.P. Anipsitakis, D.D. Dionysiou, Radical generation by the interaction of transition metals with common oxidants, *Environ. Sci. Technol.* 38 (2004) 3705–3712.
 - [11] X.B. Wang, Y.L. Qin, L.H. Zhu, H.Q. Tang, Nitrogen-doped reduced graphene oxide as a bifunctional material for removing bisphenols: synergistic effect between adsorption and catalysis, *Environ. Sci. Technol.* 49 (2015) 6855–6864.
 - [12] T.K. Lau, W. Chu, N.J.D. Graham, The aqueous degradation of butylated hydroxyanisole by UV/S₂O₈²⁻: study of reaction mechanisms via dimerization and mineralization, *Environ. Sci. Technol.* 41 (2007) 613–619.
 - [13] R.H. Waldemer, P.G. Tratnyek, R.L. Johnson, J.T. Nurmi, Oxidation of chlorinated ethenes by heat-activated persulfate: kinetics and products, *Environ. Sci. Technol.* 41 (2007) 1010–1015.
 - [14] S. Indrawirawan, H. Sun, X. Duan, S. Wang, Nanocarbons in different structural dimensions (0–3D) for phenol adsorption and metal-free catalytic oxidation, *Appl. Catal. B: Environ.* 179 (2015) 352–362.
 - [15] S. Indrawirawan, H. Sun, X. Duan, S. Wang, Low temperature combustion synthesis of nitrogen-doped graphene for metal-free catalytic oxidation, *J. Mater. Chem. A* 3 (2015) 3432–3440.
 - [16] G. Li, Y. Lu, C. Lu, M. Zhu, C. Zhai, Y. Du, P. Yang, Efficient catalytic ozonation of bisphenol-A over reduced graphene oxide modified sea urchin-like α -MnO₂ architectures, *J. Hazard. Mater.* 294 (2015) 201–208.
 - [17] L. Duan, X. Zhou, S. Liu, P. Shi, W. Yao, 3D-hierarchically structured Co₃O₄/graphene hydrogel for catalytic oxidation of Orange II solutions by activation of peroxymonosulfate, *J. Taiwan Inst. Chem.* 76 (2017) 101–108.
 - [18] G. Li, K. Li, A. Liu, P. Yang, Y. Du, M. Zhu, 3D flower-like β -MnO₂/reduced graphene oxide nanocomposites for catalytic ozonation of dichloroacetic acid, *Sci. Rep.* 7 (2017) 43643.
 - [19] Y. Liu, X. Liu, Y. Zhao, D.D. Dionysiou, Aligned α -FeOOH nanorods anchored on a graphene oxide-carbon nanotubes aerogel can serve as an effective Fenton-like oxidation catalyst, *Appl. Catal. B: Environ.* 213 (2017) 74–86.
 - [20] W.J. Tian, H.Y. Zhang, X.G. Duan, H.Q. Sun, M.O. Tade, H.M. Ang, S.B. Wang, Nitrogen- and sulfur-codoped hierarchically porous carbon for adsorptive and oxidative removal of pharmaceutical contaminants, *ACS Appl. Mater. Interfaces* 8 (2016) 7184–7193.
 - [21] C.Z. Zhu, H. Li, S.F. Fu, D. Du, Y.H. Lin, Highly efficient nonprecious metal catalysts towards oxygen reduction reaction based on three-dimensional porous carbon nanostructures, *Chem. Soc. Rev.* 45 (2016) 517–531.
 - [22] W. Xia, R.Q. Zou, L. An, D.G. Xia, S.J. Guo, A metal-organic framework route to in situ encapsulation of Co@Co₃O₄@C core@birell nanoparticles into a highly ordered porous carbon matrix for oxygen reduction, *Energy Environ. Sci.* 8 (2015) 568–576.
 - [23] D.H. Deng, L. Yu, X.Q. Chen, G.X. Wang, L. Jin, X.L. Pan, J. Deng, G.Q. Sun, X.H. Bao, Iron encapsulated within pod-like carbon nanotubes for oxygen reduction reaction, *Angew. Chem. Int. Ed.* 52 (2013) 371–375.
 - [24] J. Liang, Y. Jiao, M. Jaroniec, S.Z. Qiao, Sulfur and nitrogen dual-doped mesoporous graphene electrocatalyst for oxygen reduction with synergistically enhanced performance, *Angew. Chem. Int. Ed.* 51 (2012) 11496–11500.
 - [25] Z.S. Wu, A. Winter, L. Chen, Y. Sun, A. Turchanin, X.L. Feng, K. Mullen, Three-dimensional nitrogen and boron co-doped graphene for high-performance all-solid-state supercapacitors, *Adv. Mater.* 24 (2012) 5130–5135.
 - [26] H.Q. Sun, Y.X. Wang, S.Z. Liu, L. Ge, L. Wang, Z.H. Zhu, S.B. Wang, Facile synthesis of nitrogen doped reduced graphene oxide as a superior metal-free catalyst for oxidation, *Chem. Commun.* 49 (2013) 9914–9916.
 - [27] C. Bresson, C. Colin, F. Chartier, C. Moulin, Cobalt speciation study in the cobalt-cysteine system by electrospray ionization mass spectrometry and anion-exchange chromatography inductively coupled plasma atomic emission spectrometry, *Appl. Spectrosc.* 59 (2005) 696–705.
 - [28] W. Buchmann, R. Spezia, G. Tournois, T. Cartailier, J. Tortajada, Structures and fragmentations of cobalt(II)-cysteine complexes in the gas phase, *J. Mass Spectrom.* 42 (2007) 517–526.
 - [29] R. Sharma, K.K. Kar, Effects of structural disorder and nitrogen content on the oxygen reduction activity of polyvinylpyrrolidone-derived multi-doped carbon, *J. Mater. Chem. A* 3 (2015) 11948–11959.
 - [30] G.A. Ferrero, A.B. Fuertes, M. Sevilla, N-doped porous carbon capsules with tunable porosity for high-performance supercapacitors, *J. Mater. Chem. A* 3 (2015) 2914–2923.
 - [31] D. Puthusseri, V. Aravindan, S. Madhavi, S. Ogale, 3D micro-porous conducting carbon beehive by single step polymer carbonization for high performance supercapacitors: the magic of in situ porogen formation, *Energy Environ. Sci.* 7 (2014) 728–735.
 - [32] Y.Y. Li, F.Y. Cheng, J.N. Zhang, Z.M. Chen, Q. Xu, S.J. Guo, Cobalt-carbon core-shell nanoparticles aligned on wrinkle of N-doped carbon nanosheets with Pt-like activity for oxygen reduction, *Small* 12 (2016) 2839–2845.
 - [33] J.F. Moulder, W.F. Stickle, P.E. Sobol, K.D. Bomben, *Handbook of X-ray Photoelectron Spectroscopy: a Reference Book of Standard Spectra for Identification and Interpretation of XPS Data*, Physical Electronics, 1995.
 - [34] W. Tian, H. Zhang, H. Sun, M.O. Tade, S. Wang, Template-free synthesis of N-doped carbon with pillared-layered pores as bifunctional materials for supercapacitor and environmental applications, *Carbon* 118 (2017) 98–105.
 - [35] W. Tian, H. Zhang, H. Sun, A. Suvorova, M. Saunders, M. Tade, S. Wang, Heteroatom (N or S)-doping induced layered and honeycomb microstructures of porous carbons for CO₂ capture and energy applications, *Adv. Funct. Mater.* 26 (2016) 8651–8662.
 - [36] C. Wang, J. Kang, P. Liang, H. Zhang, H. Sun, M.O. Tade, S. Wang, Ferric carbide nanocrystals encapsulated in nitrogen-doped carbon nanotubes as an outstanding environmental catalyst, *Environ. Sci. Nano* 4 (2017) 170–179.
 - [37] H. Sun, S. Liu, G. Zhou, H.M. Ang, M.O. Tade, S. Wang, Reduced graphene oxide for catalytic oxidation of aqueous organic pollutants, *ACS Appl. Mater. Interfaces* 4 (2012) 5466–5471.
 - [38] F.C. Moreira, R.A.R. Boaventura, E. Brillas, V.J.P. Vilar, Electrochemical advanced oxidation processes: a review on their application to synthetic and real wastewaters, *Appl. Catal. B: Environ.* 202 (2017) 217–261.
 - [39] D.F. Evans, M.W. Upton, Studies on singlet oxygen in aqueous-solution. Part 3. The decomposition of peroxy-acids, *J. Chem. Soc. Dalton Trans.* (1985) 1151–1153.
 - [40] S.A. Wohlgemuth, R.J. White, M.G. Willinger, M.M. Titirici, M. Antonietti, A one-pot hydrothermal synthesis of sulfur and nitrogen doped carbon aerogels with enhanced electrocatalytic activity in the oxygen reduction reaction, *Green Chem.* 14 (2012) 1515–1523.